[ISFA2020-9611]

CLOSED-LOOP SIMULATION INTEGRATING FINITE ELEMENT MODELING WITH FEEDBACK CONTROLS IN POWDER BED FUSION ADDITIVE MANUFACTURING

Dan Wang
Dept. of Mechanical Engineering
University of Washington
Seattle, Washington, 98195
Email: daw1230@uw.edu

Xu Chen*
Dept. of Mechanical Engineering
University of Washington
Seattle, Washington, 98195
Email: chx@uw.edu

ABSTRACT

Powder bed fusion (PBF) additive manufacturing has enabled unmatched agile manufacturing of a wide range of products from engine components to medical implants. While high-fidelity finite element modeling and feedback control have been identified key for predicting and engineering part qualities in PBF, existing results in each realm are developed in opposite computational architectures wildly different in time scale. Integrating both realms, this paper builds a first-instance closed-loop simulation framework by utilizing the output signals retrieved from the finite element model (FEM) to directly update the control signals sent to the model. The proposed closed-loop simulation enables testing the limits of advanced controls in PBF and surveying the parameter space fully to generate more predictable part qualities. Along the course of formulating the framework, we verify the FEM by comparing its results with experimental and analytical solutions and then use the FEM to understand the melt-pool evolution induced by the in-layer thermomechanical interactions. From there, we build a repetitive control algorithm to greatly attenuate variations of the melt pool width.

1 Introduction

Additive manufacturing (AM) builds a part directly from its digital model by joining materials layer by layer, which is different from conventional subtractive machining. In particular, powder bed fusion (PBF) AM, applying high-precision lasers or electron beams as the energy source, has enabled unprecedented fabrication of complex parts from polymeric and metallic powder materials. However, broader adoption of the technology remains challenged by insufficient reliability and in-process variations induced by, for example, uncertain laser-material interactions, environmental vibrations, powder recycling, imperfect interactions of mechanical components, and complex thermal histories of materials [1–3].

Current researches employ finite element modeling and feedback controls to understand the energy-deposition mechanisms and to regulate the in-process variations in PBF and other AM technologies such as laser metal deposition (LMD). Particularly, [4–6] adopt finite element modeling to investigate the effects of various scan patterns, scan speeds, number of lasers, and overhanging structures on the thermal fields of the powder bed, the geometries of the melt pool, and the mechanical properties of the printed parts. Existing strategies on feedback controls often implement low-order system models obtained using system identification techniques [2, 7–9]. A nonlinear memoryless submodel [8, 10] and a spatial-domain Hammerstein model [9] have been built to cover more complicated process dynamics. From there, PID control [2, 11–13], sliding mode control [10], predictive control [7], and iterative learning control [14] have proved their efficiencies in improving the dimensional accuracy of the printed parts in PBF and LMD.

Although finite element models (FEMs) and feedback controls have been identified key for predicting and engineering part qualities in PBF, existing results in each realm are developed in separate computational architectures due to their different time
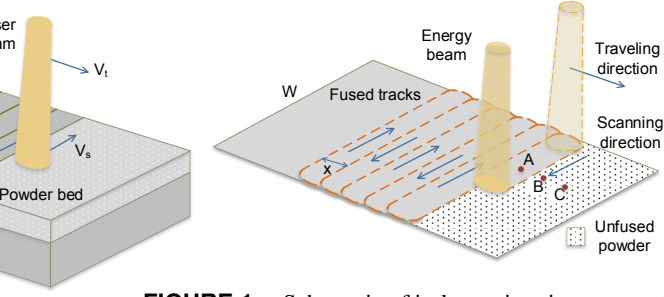
FIGURE 1. Schematic of in-layer sintering process in PBF.

scales. To be more specific, feedback controls are implemented in real time, while it can take hours or even days for FEMs to simulate the sintering of a few layers that finishes in seconds in reality. If we can integrate FEMs with feedback controls directly in a closed loop, however, we will be able to 1) combine aforementioned knowledges from each realm, 2) test the limits of advanced controls in PBF, 3) survey the parameter space fully to generate more predictable part qualities, and 4) quickly design controllers and update parameters for novel materials and printer settings. These benefits are more prominent when the experiments are costly and time-consuming.

In pursuit of the above benefits, this paper builds, in the first instance to our best knowledge, a closed-loop high-fidelity simulation framework that leverages modern architectures of finite-element-modeling tools and the power of data processing and advanced controls. Specifically, we build a bidirectional communication so that the output signals (e.g., melt pool width) retrieved from the FEM can be utilized to directly update the FEM process parameters (e.g., laser power) in external control toolboxes (e.g., MATLAB). Along the course of formulating the framework, we validate the FEM by comparing its results with experimental and analytical solutions and furthermore apply the FEM to investigate the periodic in-layer thermal interactions. Under the framework of the closed-loop simulation, we then verify the effectiveness of the repetitive control (RC) in attenuating the repetitive variations of the melt pool width.

The remainder of this paper is structured as follows. Section 2 builds the main closed-loop simulation framework taking an FEM and a plug-in RC design for example. Section 3 verifies the FEM and justifies the existence of the periodic in-layer thermal interactions. Section 4 implement the proposed closed-loop simulation to evaluate the performance of RC in attenuating the periodic in-layer disturbances. Section 5 concludes the paper.

2 Proposed high-fidelity closed-loop simulation

A typical part in PBF is built from many thousands of thin layers. Within each layer (Fig. 1), the energy beam is regulated to follow trajectories predefined by the part geometry in a slicing process. After one layer is finished printing, a new thin layer of powder will be spread on top, and then another cycle begins. This section frames the main high-fidelity closed-loop simulation. We first design an FEM to simulate the thermal fields during the PBF process. After that, a sample RC algorithm is designed and introduced to the closed-loop simulation.

2.1 FEM

We use the COMSOL Multiphysics 5.3a software to build and refine the FEM of the thermal fields in PBF. The model considers surface convection, surface radiation, conduction, and latent heat of fusion. For brevity and without loss of generality, the effects of evaporation, fluid flow, and Marangoni force are neglected. The governing equation for conduction heat flow is

$$\rho c_p \frac{dT(x,y,z,t)}{dt} = \nabla \cdot (k \nabla T(x,y,z,t)) + q_s, \quad (1)$$

where k is the thermal conductivity, c_p the specific heat capacity, ρ the effective density, t the time, T the temperature, and q_s the rate of local internal energy generated per unit volume [15]. When no confusion would arise in the context, $T(x,y,z,t)$ is abbreviated to T in the remaining of this paper.

2.1.1 Phase change and temperature-dependent thermal properties

We account for the latent heat of fusion L_f by introducing the effective heat capacity [19]:

$$c_{p,eff}(T) = \begin{cases} c_{p1}(T) & T_0 < T \leq T_{sol} \\ \frac{L_f}{T_m - T_{sol}} + \frac{c_{p1}(T_{sol}) + c_{p2}(T_m)}{2} & T_{sol} < T < T_m \\ c_{p2}(T) & T \geq T_m \end{cases} \quad (2)$$

where T_0 is the ambient temperature, T_{sol} the solidus temperature, T_m the melting point, c_{p1} the heat capacity of the powder, and c_{p2} the heat capacity of the liquid.

For the thermal properties, we adopt k, c_p, and ρ in [4, 16] for the solid and liquid materials. For the powder material, we use the thermal properties generated from the solid material by considering the porosity ϕ [17, 18]: $k_{powder} = k_{solid}(1 - \phi)^4$ and $\rho_{powder} = \rho_{solid}(1 - \phi)$, where ϕ is expressed as

$$\phi(T) = \begin{cases} \phi_0 & T_0 < T \leq T_{sol} \\ \frac{\phi_0}{T_{sol} - T_m}(T - T_m) & T_{sol} < T < T_m \\ 0 & T \geq T_m \end{cases}$$

with ϕ_0 denoting the initial porosity. Here, the heat capacity is assumed to be the same for the powder and solid materials except in $T_{sol} < T < T_m$ [17]. Fig. 2 shows the temperature-dependent thermal properties used in this paper.

FIGURE 2. Te... ...f Ti6Al4V [4,16-18]. Solid li...solid and liquid material... Dash-dotted lin...
material. Th...
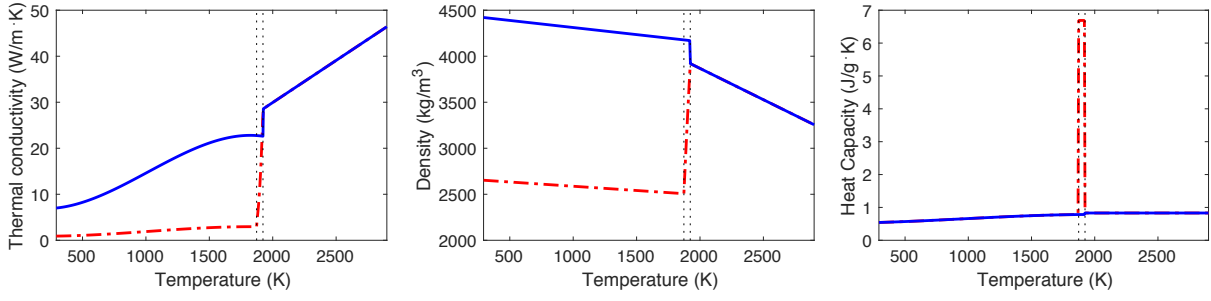
2.1.2
laser bea
One bound...
$(z = h)$ has...
dition cons...

$$-k...$$

where Q i...
coefficient...
stant. Her...

$Q \approx \frac{2q}{\pi R^2} e^{-...}$
beam radi...
center of t...
eters used...

2.1.3 Meshing and scanning schemes
plot of Fig. 3 shows the built FEM with a substrate a...
layer of powder bed. In this FEM, we use a selective...
scheme to balance model accuracy with computation ti...
quad-and-swept mesh with a maximum element size...
is applied to the central powder bed region that dire...
acts with the energy beam, whereas less finer tetrahe...
(3.5 mm) and triangular-and-swept mesh (2 mm) are a...
the substrate and the peripheral powder bed, respectively. The
left plot of Fig. 3 also illustrates the bidirectional scan scheme
used in this study with a hatch spacing (Δx in Fig. 1) of 60 μm.
The developed FEM will be verified in Section 3.

2.2 Closed-loop simulation framework
We propose here the main closed-loop simulation frame-
work that integrates feedback controls with FEM (e.g., the FEM
in Section 2.1) and enables updating directly the control signals
of the FEM. This closed-loop framework is designed using the
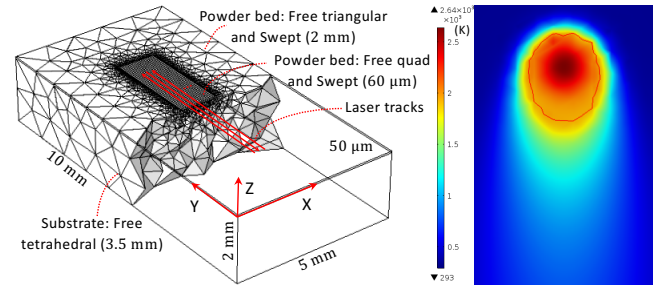
FIGURE 3. Left: powder bed and substrate with selective meshing
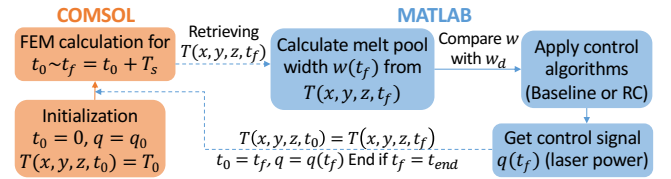
FIGURE 4. Schematic of proposed closed-loop simulation.

software *LiveLink™ for MATLAB* and mainly composed of two
parts: FEM developed using COMSOL and feedback control al-
gorithms designed using MATLAB. The key idea of this closed-
loop framework is to use the output signals retrieved from the
FEM to update in MATLAB the control signals sent back to the
model step by step. As a case study, we use melt pool width as
the output signal and laser power as the control signal.

Fig. 4 illustrates the procedures of the proposed closed-loop
simulation. First of all, we initialize the FEM in Section 2.1 by
setting the start time t_0 as 0, the laser power q as the initial one
q_0, and $T(x, y, z, t_0)$ as the ambient temperature T_0. Note that
the computation time of the FEM is set as one time step from t_0
to $t_f = t_0 + T_s$, and afterwards, MATLAB will call the FEM re-
cursively to finish the whole simulation with a longer time t_{end}.
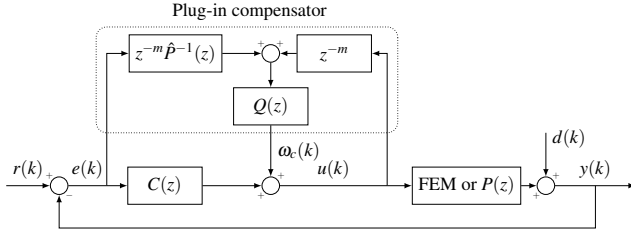The design and initialization of the FEM is completed in COM-

FIGURE 5. Block diagram of a plug-in RC design.

SOL, while the main file of the closed-loop framework is written in MATLAB. When the main file starts running, the command *model.study('std1').run* first calls COMSOL to compute the FEM (named *std1*) for one time step, and then the function *mphinterp* retrieves the temperature distribution $T(x, y, z, t_f)$ at $t = t_f$ from COMSOL. Thereafter, the main file calculates the melt pool width w at $t = t_f$ from $T(x, y, z, t_f)$ and, based on the control algorithms, processes $w(t_f)$ and obtains the control signal $q(t_f)$. At the final step, the iterative variables in the FEM are updated by assigning t_f to t_0, $T(x, y, z, t_f)$ to $T(x, y, z, t_0)$, and $q(t_f)$ to the laser power. After this iteration, MATLAB will call COMSOL again to start a new FEM computation with the updated variables, and then another cycle begins. The closed-loop simulation will stop when t_f reaches to t_{end}.

The proposed closed-loop simulation achieves updating in a closed loop the control signals of FEM. This simulation framework will benefit and guide experiments by validating beforehand the effectiveness of the servo designs. Next we will bring a RC algorithm into the proposed closed-loop simulation.

2.3 Repetitive controller design

RC is designed for tracking/rejecting periodic exogenous references/disturbances in applications with repetitive tasks [20]. By learning from previous iterations, RC can greatly enhance current control performance in the structured task space. In digital RC, an internal model $1/(1 - z^{-N})$ is incorporated in the controller, where z is the complex indeterminate in the z-transform. $N = f_s/f_0$ is the period of the signal, where $f_s = 1/T_s$ is the sampling frequency and f_0 is the fundamental disturbance frequency. Consider a baseline feedback system consisting a plant $P(z)$ and a baseline controller $C(z)$ (Fig. 5 with the dotted box removed). Here, $C(z)$ can be designed by conventional servo algorithms, such as PID, H_∞, and lead-lag compensation. The signals $r(k)$, $d(k)$, $u(k)$, and $y(k)$ respectively represent the reference, the input disturbance, the control signal, and the system output. The sensitivity function $S(z) = \frac{1}{1 + P(z)C(z)}$ is the transfer function from $d(k)$ to $y(k)$.

We introduce here a plug-in RC design [21] that uses the internal signals $e(k)$ and $u(k)$ to generate a compensation signal $\omega_c(k)$ (Fig. 5). Let m denote the relative degree of $\hat{P}(z)$, where

$\hat{P}(z)$ is the nominal model of $P(z)$. The transfer function of the overall controller from $e(k)$ to $u(k)$ is

$$C_{all}(z) = \frac{C(z) + z^{-m}\hat{P}^{-1}(z)Q(z)}{1 - z^{-m}Q(z)}. \qquad (4)$$

The internal model is integrated in C_{all} by designing the Q filter as $Q(z) = (1 - \alpha^N)z^{m-N}/(1 - \alpha^N z^{-N})$, which gives $1 - z^{-m}Q(z) = (1 - z^{-N})/(1 - \alpha^N z^{-N})$, where $\alpha \in [0, 1)$ is a tuning factor. At the harmonic frequencies $\omega_k = k2\pi f_0 T_s$ ($k \in \mathbb{Z}^+$), with $z = e^{j\omega_k}$, we have $1 - z^{-N} = 0$, $1 - z^{-m}Q(z) = 0$, $C_{all}(z) \to \infty$ from (4), and hence the new sensitivity function $S_0(z) = \frac{1}{1 + P(z)C_{all}(z)} = 0$. At the intermediate frequencies $\omega \neq k2\pi f_0 T_s$, with $z = e^{j\omega}$ and α being close to 1, $Q(z) \approx 0$, $1 - z^{-m}Q(z) \approx 1$, $C_{all}(z) \approx C(z)$ from (4), and thereby the original loop shape is maintained.

During implementation, zero-phase pairs $q_0(z^{-1})q_0(z)$ are attached to $Q(z)$ for robustness against high-frequency plant uncertainties:

$$Q(z) = \frac{(1 - \alpha^N)z^{m-N}}{1 - \alpha^N z^{-N}} q_0(z^{-1})q_0(z), \qquad (5)$$

where $q_0(z) = (1 + z)^{n_0}/2^{n_0}$ and $n_0 \in \mathbb{Z}^+$. The closed-loop performance $S_0(z)$ can be tuned by choosing different α and n_0 [21]. The plug-in RC and the baseline control can be easily incorporated into the closed-loop simulation by setting $u(k)$ as $q(t_f)$ and $y(k)$ as $w(t_f)$. Under the framework of the closed-loop simulation, we will prove in Section 4 the effectiveness of RC in PBF.

3 Model verification and thermal interactions

In this section, we verify the FEM in Section 2.1 and then apply it to understand the periodic in-layer thermal cycles.

3.1 Model verification

We compare the melt pool widths obtained from the FEM first with the experimental results and then with the analytical solutions. Throughout this paper, melt pool widths are derived from the temperature distribution (e.g., $T(x, y, z, t)$ in the FEM) by searching around the position of the laser beam to find the maximum width of the melt pool geometry bounded by T_m.

We compare in Table 1 the numerical melt pool widths with the experimental results in [22]. The laser power is fixed to 50 W, and the scan speed is 100, 200, or 300 mm/s. Overall, the FEM gives reasonable predictions of the melt pool widths with errors of 3.61%, 6.41%, and 5.44%, respectively. The main reason that the numerical melt pool widths are slightly (less than 10 μm) larger than the experimental results is that evaporation is ignored

TABLE 1. Melt pool widths from FEM and experimental results [22] with a fixed laser power of 50 W. Difference=FEM-Experiments. Error=(FEM-Experiments)/FEM.

Scan speed (mm/s)	100	200	300
FEM (μm)	182	152.63	132.56
Experiments (μm) Min/Max	165.71/175.43	140.71/142.85	120.71/125.35
Difference (μm)	6.57	9.78	7.21
Error	3.61%	6.41%	5.44%
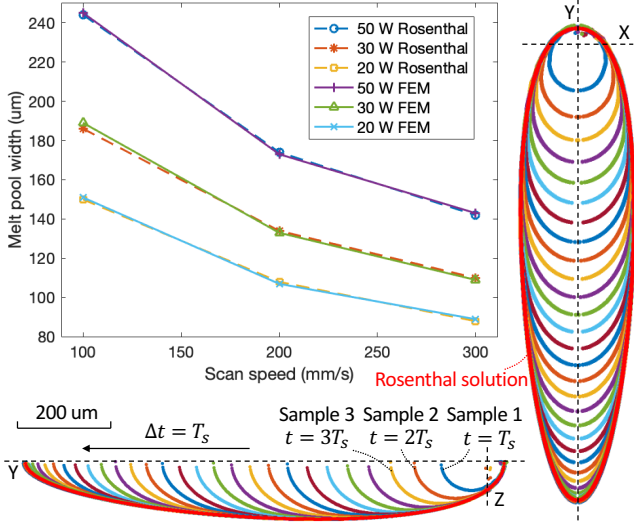
FIGURE 6. Melt pool widths from the FEM and analytical solution. Right and bottom left plots share the same scale and legend.

in the FEM so the overheated material and the heat within are condensed in the melt pool.

Then we compare the FEM results with the analytical solutions. When a moving point laser source is acting on a thick plate and the thermal properties of the plate are constant, the analytical solution of (1) in the steady state is the Rosenthal equation [15]: $T(\xi, y, z) - T_0 = \frac{q}{2\pi k r} e^{-\frac{u_x(r+\xi)}{2\kappa}}$, where (ξ, y, z) is a coordinate system attached to the moving source, $r = \sqrt{\xi^2 + y^2 + z^2}$, and $\kappa = k/(\rho c_p)$. For comparison, the FEM is adapted to accommodate the assumptions of the Rosenthal equation, such as constant thermal properties ($k = 5$ W/(m·K), $c_p = 1.1$ J/(g·K), and $\rho = 4300$ kg/m^3) and point heat source. Fig. 6 compares the numerical and analytical solutions. As shown in the right plot and the bottom left plot, after 27 samples, the numerical melt pool geometry reaches to the steady state and matches with the Rosenthal solution (the outline). Also, from the top left plot of Fig. 6, we can tell that the melt pool widths obtained from the FEM and the Rosenthal equation match well with each other under different combinations of scan speeds and laser powers.
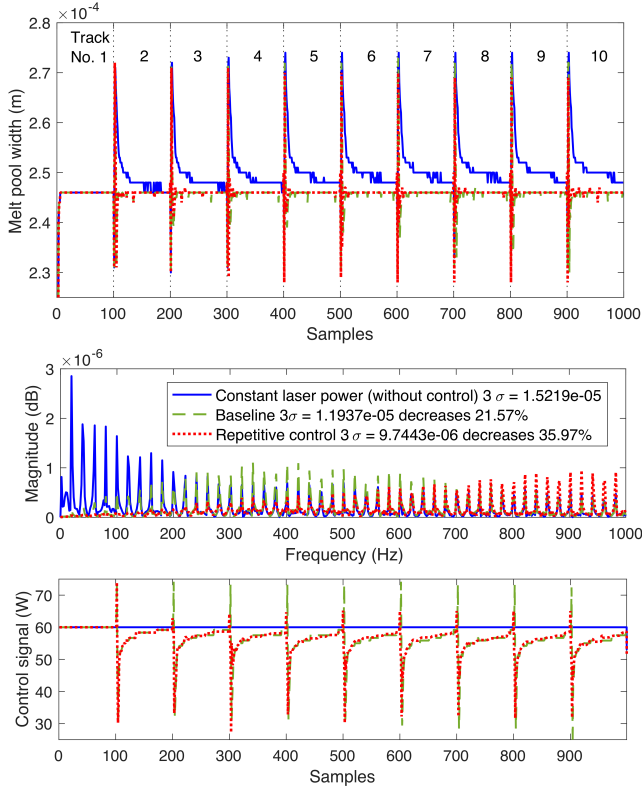
3.2 Periodic thermal interactions

After having validated the FEM, next we will adopt it to investigate the periodic in-layer thermal cycles in PBF. Here, we bidirectionally sinter 10 tracks within one layer (Figs. 1 and 3). The right plot in Fig. 3 illustrates the simulated surface temperature distribution at $t = 0.14$ s, where the isotherm of $T = T_m$ indicates the melt pool geometry. From the solid line in the top plot of Fig. 7, we observe that the melt pool width changes over time and structurally deviates from the steady-state value 246 μm extracted from the first track. Most importantly, the start of each track has larger melt pool widths than the rest of the track. This is because in bidirectional scanning, when the energy beam approaches the end of one track, the large latent heat does not have enough time to dissipate out before the next track starts. The resulting increased melt pool widths at the beginning of each track form a periodic disturbance with a repetitive spectrum in the frequency domain (the solid line in the middle plot of Fig. 7). The fundamental frequency f_0 of the disturbance is determined by the duration of scanning one track t_0, that is, $f_0 = 1/t_0 = u_x/L$, where u_x is the scan speed and L is the track length. In this example, $f_0 = 100/5 = 20$ Hz, and frequency spikes at $n f_0$ ($n \in \mathbb{Z}^+$, the set of positive integers) appear in the fast Fourier transform (FFT) of the disturbance.

The disturbance periodicity is closely related to the recurring laser scanning trajectories and the repetitive in-layer thermomechanical interactions. Besides the bidirectional scan used in this study, other scan patterns yield similar repetitive disturbances (see, e.g., experimental results in [23]). To deal with these undesired repetitive spectra, we implement the closed-loop simulation by bringing automatic control algorithms [1, 21] into finite element modeling, as will be discussed in Section 4.
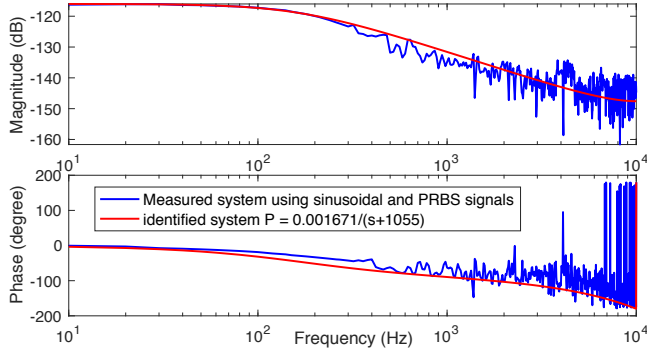
4 Results and Analyses

This section employs the proposed closed-loop simulation to evaluate the performances of the baseline control and RC in attenuating the variations of the melt pool width (Section 3.2). First, we identify the plant model of the FEM from the laser power to the melt pool width as $P(s) = 0.001671/(s + 1055)$. The input signals used for system identification include a pseudorandom binary sequence (PRBS) signal and multiple sinusoidal signals (10~300 Hz), with magnitudes of 20 W and add-on DC components of 60 W. The frequency responses of the measured and identified systems match well with each other (see Fig. 8).

After that, we design a PI controller as $C(s) = K_p + K_i/s$ with $K_p = 9.38 \times 10^5$ and $K_i = 1.66 \times 10^9$. Under the sampling time T_s of 0.5 ms (i.e., $f_s = 2$ kHz), the zero-order-hold equivalents of the plant and controller models respectively are $P(z) = 6.493 \times 10^{-7}/(z - 0.5901)$ and $C(z) = (9.38z - 1.08) \times 10^5/(z - 1)$. The dashed line in Fig. 9 shows the magnitude response of the sensitivity function $S(z)$ in the baseline feedback loop composed of $P(z)$ and $C(z)$. Such a design provides a band-
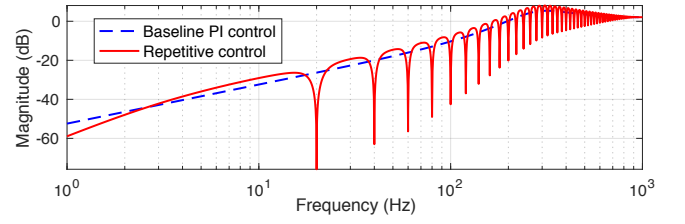
FIGURE 7. In-layer thermal disturbance. Top: time-domain. Middle: frequency-domain (FFT). Bottom: laser power (control signals $u(k)$ in Fig. 5). The three plots share the same legend. σ denotes the standard deviation.

FIGURE 8. Measured and identified system responses.

FIGURE 9. Magnitude responses of sensitivity functions $S(z)$ in baseline control and $S_0(z)$ in RC.

to some extent the frequency spikes below the closed-loop bandwidth but not the other high-frequency spikes. Compared to the case without control, the baseline feedback loop decreases the 3σ value of the variations of the melt pool width ($y(k)$ in Fig. 5) by 21.57%, where σ denotes the standard deviation.

To enhance the disturbance-attenuation performance, we bring the plug-in RC compensator in Section 2.3 into the closed-loop simulation. In the Q-filter design in (5), the relative degree m of $\hat{P}(z)(= P(z)$ in this example) is 1, the disturbance period $N = f_s/f_0 = 2000/20 = 100$, and we choose $\alpha = 0.99$ and $n_0 = 1$. With the plug-in RC introduced, high-gain control efforts are generated exactly at 20 Hz and its harmonics (see $S_0(z)$ in the solid line of Fig. 9). The bottom plot of Fig. 7 illustrates the control signals $u(k)$ of the baseline control, the RC, and the case without control. As shown in the middle plot of Fig. 7, compared with the baseline control, RC further lowers the periodic frequency spikes especially at high frequencies beyond the closed-loop bandwidth and decreases the 3σ value by 35.97%. Similarly, in the time domain, the increased control efforts of RC at the harmonic frequencies yield a further-attenuated output $y(k)$ (the top plot of Fig. 7).

5 Conclusion

In this paper, we first build a finite element model (FEM) to simulate the temperature response in powder bed fusion (PBF) additive manufacturing. Then we validate the FEM by comparing the numerical results with the experimental and analytical solutions. Employing the FEM, we justify the existence of the periodic disturbances in the evolution of the melt pool width. From there, we develop a first-instance closed-loop simulation framework by integrating FEM with feedback controls (e.g., baseline PI control and repetitive control) to reduce the in-process variations and advance the part quality in PBF. Implementing this closed-loop frameworks, we validate that the repetitive control algorithm attenuates the periodic disturbances more substantially by 35.97% compared to the PI control.

width at 197 Hz, which approximates the limit of 20% of the Nyquist frequency (1000 Hz) and indicates that the PI controller is well tuned. The closed-loop simulations are designed according to Section 2.2 integrating FEM with baseline control and RC, respectively. Here, in Fig. 5, $r(k) = 0$, and $d(k)$ comes from the in-layer thermal interactions. From the frequency-domain results in Fig. 7, we can tell that the baseline PI control can attenuate

Acknowledgment

Appendix: defined parameters of the FEM

Parameters	Value	Parameters	Value
Powder bed size	$5\,\text{mm} \times 10\,\text{mm} \times 50\,\mu\text{m}$	Material	Ti6Al4V
Substrate size	$5\,\text{mm} \times 10\,\text{mm} \times 2\,\text{mm}$	Track length L	$5\,\text{mm}$
Laser spot diameter $2R$	$220\,\mu\text{mm}$	Time step T_s	$0.5\,\text{ms}$
Powder bed absorptance	0.25	Emissivity	0.35
Solidus temperature T_{sol}	1873 K	Scan speed u_x	$100\,\text{mm/s}$
Latent heat of fusion L_f	295 kJ/kg	Laser power q	60 W
T_0/T_m	293.15 K/1923.15 K	ϕ_0	0.4
h_c	$12.7\,\text{W/(m}^2\cdot\text{K)}$	k, c_p, and ρ	Fig. 2

References

[1] D. Wang and X. Chen, "A multirate fractional-order repetitive control for laser-based additive manufacturing," *Control Engineering Practice*, vol. 77, pp. 41–51, 2018.

[2] J.-P. Kruth, P. Mercelis, J. Van Vaerenbergh, and T. Craeghs, "Feedback control of selective laser melting," in *Proceedings of the 3rd international conference on advanced research in virtual and rapid prototyping*, 2007, pp. 521–527.

[3] V. Seyda, N. Kaufmann, and C. Emmelmann, "Investigation of aging processes of ti-6al-4 v powder material in laser melting," *Physics Procedia*, vol. 39, pp. 425–431, 2012.

[4] M. Masoomi, S. M. Thompson, and N. Shamsaei, "Laser powder bed fusion of ti-6al-4v parts: Thermal modeling and mechanical implications," *International Journal of Machine Tools and Manufacture*, vol. 118, pp. 73–90, 2017.

[5] A. Hussein, L. Hao, C. Yan, and R. Everson, "Finite element simulation of the temperature and stress fields in single layers built without-support in selective laser melting," *Materials & Design (1980-2015)*, vol. 52, pp. 638–647, 2013.

[6] A. Foroozmehr, M. Badrossamay, E. Foroozmehr *et al.*, "Finite element simulation of selective laser melting process considering optical penetration depth of laser in powder bed," *Materials & Design*, vol. 89, pp. 255–263, 2016.

[7] L. Song and J. Mazumder, "Feedback control of melt pool temperature during laser cladding process," *IEEE Transactions on Control Systems Technology*, vol. 19, no. 6, pp. 1349–1356, 2011.

[8] X. Cao and B. Ayalew, "Control-oriented mimo modeling of laser-aided powder deposition processes," in *American Control Conference (ACC), 2015*. IEEE, 2015, pp. 3637–3642.

[9] P. M. Sammons, D. A. Bristow, and R. G. Landers, "Repetitive process control of laser metal deposition," in *ASME 2014 Dynamic Systems and Control Conference*. American Society of Mechanical Engineers, 2014, pp. V002T35A004–V002T35A004.

[10] A. Fathi, A. Khajepour, M. Durali, and E. Toyserkani, "Geometry control of the deposited layer in a nonplanar laser cladding process using a variable structure controller," *Journal of manufacturing science and engineering*, vol. 130, no. 3, p. 031003, 2008.

[11] J. Hofman, B. Pathiraj, J. Van Dijk, D. de Lange, and J. Meijer, "A camera based feedback control strategy for the laser cladding process," *Journal of Materials Processing Technology*, vol. 212, no. 11, pp. 2455–2462, 2012.

[12] D. Salehi and M. Brandt, "Melt pool temperature control using labview in nd: Yag laser blown powder cladding process," *The international journal of advanced manufacturing technology*, vol. 29, no. 3, pp. 273–278, 2006.

[13] A. Fathi, A. Khajepour, E. Toyserkani, and M. Durali, "Clad height control in laser solid freeform fabrication using a feedforward pid controller," *The International Journal of Advanced Manufacturing Technology*, vol. 35, no. 3, pp. 280–292, 2007.

[14] L. Tang and R. G. Landers, "Layer-to-layer height control for laser metal deposition process," *Journal of Manufacturing Science and Engineering*, vol. 133, no. 2, p. 021009, 2011.

[15] E. Kannatey-Asibu Jr, *Principles of laser materials processing*. John Wiley & Sons, 2009, vol. 4.

[16] A. N. Arce, *Thermal modeling and simulation of electron beam melting for rapid prototyping on Ti6Al4V alloys*. North Carolina State University, 2012.

[17] K. Karayagiz, A. Elwany, G. Tapia, B. Franco, L. Johnson, J. Ma, I. Karaman, and R. Arróyave, "Numerical and experimental analysis of heat distribution in the laser powder bed fusion of ti-6al-4v," *IISE Transactions*, vol. 51, no. 2, pp. 136–152, 2019.

[18] J. Yin, H. Zhu, L. Ke, W. Lei, C. Dai, and D. Zuo, "Simulation of temperature distribution in single metallic powder layer for laser micro-sintering," *Computational Materials Science*, vol. 53, no. 1, pp. 333–339, 2012.

[19] I. Yadroitsev, *Selective laser melting: Direct manufacturing of 3D-objects by selective laser melting of metal powders*. LAP LAMBERT Academic Publishing, 09 2009.

[20] T. Inoue, M. Nakano, T. Kubo, S. Matsumoto, and H. Baba, "High accuracy control of a proton synchrotron magnet power supply," *IFAC Proceedings Volumes*, vol. 14, no. 2, pp. 3137–3142, 1981.

[21] X. Chen and M. Tomizuka, "New repetitive control with improved steady-state performance and accelerated transient," *IEEE Transactions on Control Systems Technology*, vol. 22, no. 2, pp. 664–675, 2014.

[22] I. Yadroitsev, P. Krakhmalev, and I. Yadroitsava, "Selective laser melting of ti6al4v alloy for biomedical applications: Temperature monitoring and microstructural evolution," *Journal of Alloys and Compounds*, vol. 583, pp. 404–409, 2014.

[23] A. J. Dunbar, E. R. Denlinger, M. F. Gouge, T. W. Simpson, and P. Michaleris, "Comparisons of laser powder bed fusion additive manufacturing builds through experimental in situ distortion and temperature measurements," *Additive Manufacturing*, vol. 15, pp. 57–65, 2017.